APPLIED GEOPHYSICS, Vol.20, No.1 (March 2023), P. 1−13, 13 Figures.
DOI:10.1007/s11770-023-1009-z

# 2D Laplace–Fourier domain acoustic wave equation modeling with an optimal finite-difference method

Wang Jing-Yu[1,2], Fan Na[1,2]*, Chen Xue-Fei[2], Zhong Shou-Rui[2], Li Bo-Yu[2], Li Dan[2], Zhao Gang[2]

**Abstract**: Laplace–Fourier (L-F) domain finite-difference (FD) forward modeling is an important foundation for L-F domain full-waveform inversion (FWI). An optimal modeling method can improve the efficiency and accuracy of FWI. A flexible FD stencil, which requires pairing and centrosymmetricity of the involved gridpoints, is used on the basis of the 2D L-F domain acoustic wave equation. The L-F domain numerical dispersion analysis is then performed by minimizing the phase error of the normalized numerical phase and attenuation propagation velocities to obtain the optimization coefficients. An optimal FD forward modeling method is finally developed for the L-F domain acoustic wave equation and applied to the traditional standard 9-point scheme and 7- and 9-point schemes, where the latter two schemes are used in discontinuous-grid FD modeling. Numerical experiments show that the optimal L-F domain FD modeling method not only has high accuracy but can also be applied to equal and unequal directional sampling intervals and discontinuous-grid FD modeling to reduce computational cost.
**Keywords**: Laplace–Fourier domain, 2D acoustic wave equation, finite difference, and optimization coefficients.

## Introduction

Full-waveform inversion (FWI), which is an important method for detecting the structure of the earth, can be implemented in the time domain (e.g., Tarantola, 1984; Bleistein et al., 1987; Yang et al., 2015; Choi and Alkhalifah, 2011), frequency domain (e.g., Pratt and Worthington, 1988; Pratt et al., 1998; Song et al., 1995; Pratt, 1999; Sirgue and Pratt, 2004), the Laplace domain (e.g., Shin and Cha, 2008; Bae et al., 2010; Ha et al., 2012) and Laplace–Fourier (L-F) domain (e.g., Shin and Cha, 2009; Shin et al., 2010). Time- and frequency-domain FWIs are widely studied, and each domain has its advantages and disadvantages (Vigh and Starr, 2008; Virieux and Operto, 2009). Laplace and L-F domain FWIs are essentially expanded from the frequency-domain FWI. These two FWIs are proposed to solve the failure of the conventional frequency-domain FWIs to recover large-scale subsurface structures due to the limited low-frequency information. Frequency-domain FWI uses the full real-frequency components of the

Manuscript received by the Editor September 10, 2021; revised manuscript received May 20, 2022.
1. Key Laboratory of Exploration Technologies for Oil and Gas Resources (Yangtze University), Ministry of Education, Wuhan 430100, China.
2. School of Geophysics and Oil Resources, Yangtze University, Wuhan 430100, China.
*Corresponding author: Fan Na (Email: fanna@yangtzeu.edu.cn).

elastic or acoustic wavefield. This inversion cannot converge to the real model when the initial model has a considerable difference from the real model. Laplace-domain FWI first introduces the damping wavefield and uses only the zero frequency component of the damped wavefield to reconstruct the long wavelength structure. L-F domain FWI further uses full frequency components of the damped wavefield, including the low-frequency components. The preliminary large-scale structure can provide an initial model for subsequent high-frequency inversion, thus increasing the stability of the inversion process and providing accurate results (Shin et al., 2010). L-F domain FWI not only includes the advantages of the frequency-domain FWI but also improves the low-frequency information to increase the convergence during the inversion. Their essential difference lies in the use of real and complex frequencies by the frequency and L-F domains (Cao and Chen, 2014).

FD modeling plays an important role in FWI. For frequency-domain finite-difference (FDFD) modeling, many researchers have proposed FDFD optimal methods, such as rotated FDFD operators (e.g., Jo et al., 1996; Hustedt et al., 2004; Cao and Chen, 2012; Operto et al., 2007; Operto et al., 2009; Operto et al., 2014), weighted-average method (e.g., Min et al., 2000; Gu et al., 2013; Yang and Mao, 2016), the average derivative method (ADM) (e.g., Chen, 2012; Chen and Cao, 2016, 2018; Tang et al., 2015; Zhang Heng et al., 2014), and general optimized FDFD operator, which can work with different FDFD stencils (Fan et al., 2017; Fan et al., 2018). Considering L-F domain FD modeling, which is also the key computational kernel of L-F domain FWI, the early approach was directly adapting the corresponding frequency-domain FD operators (Shin and Cha, 2009). However, the dispersion analysis of the L-F domain schemes is more complex than that of the frequency-domain (Um et al., 2012). Dispersion analysis in frequency-domain FD modeling usually involves the substitution of a plane wave into the wave equation discretized by FDFD schemes to derive the expression of numerical phase velocity and then minimize it obtain the optimization coefficients and the minimum number of sampling points per wavelength (Jo et al., 1996; Chen, 2012). For dispersion analysis in the Laplace domain, Chen (2014b) used numerical attenuation propagation velocity instead of numerical phase velocity to determine the optimization coefficients and the minimum number of sampling points per pseudo-wavelength. Moreover, for the dispersion analysis in L-F domain modeling, the numerical phase and numerical attenuation propagation velocities are employed to determine the optimization coefficients and the minimum sampling points for each wavelength and pseudo-wavelength (Chen, 2014a, 2016). Therefore, implementing the dispersion analysis of the L-F domain FD operator before the L-F domain FWI is necessary.

An optimal FD method with flexible stencil is developed in this study to solve the 2D L-F domain acoustic wave equation. The optimal method can work not only with a rectangle grid with different aspect ratios but also with a spatially discontinuous grid to reduce the computation cost. The optimization coefficients are obtained by performing the L-F domain dispersion analysis proposed by Chen (2014a). Finally, three numerical experiments are presented to validate the optimal FD modeling method in the L-F domain.

# Theory

## Finite-difference operator

The 2D Laplace–Fourier (L-F) domain acoustic wave equation can be expressed as

$$\frac{\partial^2 P}{\partial x^2}+\frac{\partial^2 P}{\partial z^2}-\frac{s^2}{v^2}P=0, \tag{1}$$

where $P$ is the displacement, $s=\sigma+i\omega$ is the complex frequency during L-F transformation, and $v$ is the acoustic velocity. As shown in Figure 1, a flexible FD stencil is used to approximate the equation, and the involved gridpoint requires pairing and centrosymmetricity. The traditional standard 9- and 25- point schemes can be regarded as special cases of Figure 1 (Fan et al., 2021). At gridpoint $P_{0,0}$, $\partial^2P/\partial z^2$ and $\partial^2P/\partial x^2$ can be approximated using surrounding $Nx\times Nz$ gridpoints by

$$\begin{aligned}\frac{\partial^2 P}{\partial x^2}&\approx\frac{1}{\Delta x^2}\sum_{n=0}^{N_z}\sum_{m=F(n)}^{N_x}c_{m,n}\left(P_{+m,+n}+P_{-m,-n}\right)\\ \frac{\partial^2 P}{\partial z^2}&\approx\frac{1}{\Delta z^2}\sum_{n=0}^{N_z}\sum_{m=F(n)}^{N_x}d_{m,n}\left(P_{+m,+n}+P_{-m,-n}\right)\end{aligned}, \tag{2}$$

where $P_{\pm m,\pm n}=P\left(\pm m\Delta x,\pm n\Delta z\right)$ and its location is shown in Figure 1. $\Delta x$ and $\Delta z$ are the spatial sampling intervals in the x- and z-directions, respectively. $F(n)=\begin{cases}0, & \text{if } n=0\\ -N_x, & \text{if } n\neq 0\end{cases}$ and $d_{m,n}$ are the

weighting coefficients for the spatial derivatives and satisfy $\sum_{n=0}^{N_z}\sum_{m=F(n)}^{N_x} c_{m,n}=0$ and $\sum_{n=0}^{N_z}\sum_{m=F(n)}^{N_x} d_{m,n}=0$, respectively. The mass acceleration term can be approximated by

$$\frac{s^2}{v^2}P=\frac{s^2}{v^2}\sum_{n=0}^{N_z}\sum_{m=F(n)}^{N_x} b_{m,n}\left(P_{+m,+n}+P_{-m,-n}\right), \tag{3}$$

where $\sum_{n=0}^{N_z}\sum_{m=F(n)}^{N_x} b_{m,n}=1/2$ $(b_{m,n}\geq 0)$. Equations (2) and (3) are then substituted into (1), and the following is obtained:

$$\begin{aligned}&\frac{1}{\Delta x^2}\sum_{n=0}^{N_z}\sum_{m=F(n)}^{N_x} c_{m,n}\left(P_{+m,+n}+P_{-m,-n}\right)\\&+\frac{1}{\Delta z^2}\sum_{n=0}^{N_z}\sum_{m=F(n)}^{N_x} d_{m,n}\left(P_{+m,+n}+P_{-m,-n}\right)\\&-\frac{s^2}{v^2}\sum_{n=0}^{N_z}\sum_{m=F(n)}^{N_x} b_{m,n}\left(P_{+m,+n}+P_{-m,-n}\right)=0\end{aligned} \tag{4}$$

Let $R=\Delta x/\Delta z$ be the aspect ratio, $a_{m,n}=c_{m,n}+R^2 d_{m,n}$, and the above equation turns into

$$\begin{aligned}&\frac{1}{\Delta x^2}\sum_{n=0}^{N_z}\sum_{m=F(n)}^{N_x} a_{m,n}\left(P_{+m,+n}+P_{-m,-n}\right)\\&-\frac{s^2}{v^2}\sum_{n=0}^{N_z}\sum_{m=F(n)}^{N_x} b_{m,n}\left(P_{+m,+n}+P_{-m,-n}\right)=0,\end{aligned} \tag{5}$$

where $\sum_{n=0}^{N_z}\sum_{m=F(n)}^{N_x} a_{m,n}=0$.

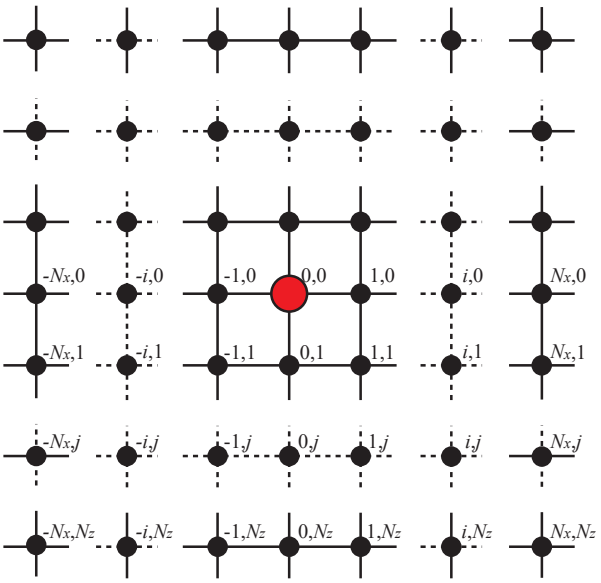


**Figure 1. Schematic of 2D L-F domain FD stencil**

## Dispersion analysis

The optimization coefficients are calculated following the L-F domain dispersion analysis of (Chen, 2014a). An attenuating plane wave $P(x,z,k)=P_0 e^{i(kx\sin\theta+kz\cos\theta)}$ is substituted into Equation (5), where $k=k_r+ik_i$ is the wavenumber, $k_r=\omega/v$ is the real wave number, $k_i=\sigma/v$ is the pseudowavenumber, and $\theta$ is the propagation angle. The discrete dispersion relation is obtained as

$$\left(\frac{s}{v}\right)^2=\frac{1}{\Delta x^2}\frac{\sum_{n=0}^{N_z}\sum_{m=F(n)}^{N_x} a_{m,n}T_{m,n}}{\sum_{n=0}^{N_z}\sum_{m=F(n)}^{N_x} b_{m,n}T_{m,n}}, \tag{6}$$

where $T_{m,n}=\cos[2\pi(m\sin\theta+n\cos\theta/r)(1/G_r+1/G_i)]$, $G_r$ and $G_i$ are the numbers of gridpoints per wavelength and per pseudo-wavelength, respectively. When $\Delta x\neq\Delta z$, the definitions of $G_r$ and $G_i$ are related to the maximum sampling interval max($\Delta x$, $\Delta z$). If $R\geq 1$, that is, $\Delta x\geq\Delta z$, then $G_r=2\pi/(k_r\Delta x)$ and $G_i=2\pi/(k_i\Delta x)$. If $R<1$, that is, Dx < $\Delta$z, then $G_r=2\pi/(k_r\Delta z)$ and $G_i=2\pi/(k_i\Delta z)$. Only the case of $R\geq 1$ ($\Delta x\geq\Delta z$) is investigated in this paper because the dispersion analysis for the case of R < 1 is similar to that of $R\geq 1$. The optimization coefficients for R < 1 can be analyzed by exchanging the x- and z-directions of the case of R ≥ 1 (Chen, 2014a; Fan et al., 2017).

The square root of equation (6) is taken. Let $F_r$ and $F_i$ represent the real and imaginary parts of the term with square root, respectively, and the following can then be obtained:

$$\frac{\omega-i\sigma}{v}=\frac{1}{\Delta x}\sqrt{-\frac{\sum_{n=0}^{N_z}\sum_{m=F(n)}^{N_x} a_{m,n}T_{m,n}}{\sum_{n=0}^{N_z}\sum_{m=F(n)}^{N_x} b_{m,n}T_{m,n}}}=\frac{1}{\Delta x}\left(F_r-iF_i\right). \tag{7}$$

Therefore, the normalized numerical phase velocity and numerical attenuation propagation velocity can be respectively expressed as follows:

$$\frac{v_r}{v}=\frac{G_r}{2\pi}F_r, \tag{8a}$$

$$\frac{v_i}{v}=\frac{G_i}{2\pi}F_i. \tag{8b}$$

The above equations represent the numerical dispersion of real- and pseudo-wavelength components. Finally, the coefficients $a_{m,n}$ and $b_{m,n}$ are determined by minimizing the following velocity error:

$$E\left(a_{m,n},b_{m,n}\right)=\iiint\left[\left(1-\frac{v_r}{v}\right)^2+\left(1-\frac{v_i}{v}\right)^2\right]d\tilde{k}_r d\tilde{k}_i d\theta, \quad (9)$$

where $\tilde{k}_r=1/G_r$ and $\tilde{k}_i=1/G_i$. The range of $\tilde{k}_r$ and $\tilde{k}_i$ depends on the number of involved gridpoints and their distribution in the scheme. The involvement of additional gridpoints requires the use of a large range. Given an FD scheme, the range of $\tilde{k}_r$ and $\tilde{k}_i$ are set by considering the tradeoff between the wavenumber coverage and the allowed phase-velocity error as well (Chen, 2014; Fan et al., 2017). Meanwhile, the range of $\theta$ is always [0, $\theta$/2].

In addition, $c_{m,n}$ and $d_{m,n}$ must be determined due to the implementation of absorption boundary conditions, such as PML. They can be obtained by minimizing the following objective function (Fan et al., 2017):

$$E\left(c_{m,n},d_{m,n}\right)=\iiint\left(E_1^{\,2}+E_2^{\,2}\right)d\tilde{k}_r d\tilde{k}_i d\theta, \quad (10)$$

where $E_1=\dfrac{\sum_{n=0}^{N_z}\sum_{m=F(n)}^{N_x}c_{m,n}T_{m,n}}{\sum_{n=0}^{N_z}\sum_{m=F(n)}^{N_x}b_{m,n}T_{m,n}}+\left[2\pi\sin\theta\left(\dfrac{1}{G_r}+\dfrac{i}{G_i}\right)\right]^2$ and

$E_2=\dfrac{\sum_{n=0}^{N_z}\sum_{m=F(n)}^{N_x}d_{m,n}T_{m,n}}{\sum_{n=0}^{N_z}\sum_{m=F(n)}^{N_x}b_{m,n}T_{m,n}}+\left[\dfrac{2\pi\cos\theta}{r}\left(\dfrac{1}{G_r}+\dfrac{i}{G_i}\right)\right]^2$.

The ranges of $k_r$, $k_i$, and $\theta$ are the same with equation (9).

The essential difference between the L-F, frequency, and Laplace domains lies in the difference in complex frequency (Cao and Chen, 2014). The frequency and Laplace domains can be regarded as special cases of the L-F domain. When the complex frequency satisfies $\sigma = 0$, $\omega \neq 0$ (i.e., $s = i\omega$), then the above optimization method in the L-F domain becomes that in the frequency domain. Only $G_r$ exists and $G_i$ disappears During dispersion analysis. When $\sigma \neq 0$, $\omega = 0$, (i.e., $s = \sigma$), the above optimization method becomes that in the Laplace domain. Meanwhile, only $G_i$ exists and $G_r$ disappears during the dispersion analysis.

The L-F domain-optimal FD method can include a previous L-F domain FD scheme as special cases. The following can be assigned:

$$c_{0,0}=-2/3,\ c_{1,0}=2/3,c_{1,1}=1/6,c_{0,1}=-1/3,\ c_{-1,1}=1/6,$$

$$d_{0,0}=-2/3,\ d_{1,0}=-1/3,\ d_{1,1}=1/6,\ d_{0,1}=2/3,\ d_{-1,1}=1/6,$$

$$b_{0,0}=1/2,\ b_{1,0}=0,\ b_{1,1}=0,\ b_{0,1}=0,\ b_{-1,1}=0,$$

Equation (4) becomes the L-F domain FD scheme adopted by Shin et al. (2002) and Shin and Cha (2009). Compared with the ADM scheme in Chen (2014a), the following can be assigned:

$$c_{0,0}=-\alpha^{Chen},c_{1,0}=\alpha^{Chen},c_{1,1}=\left(1-\alpha^{Chen}\right)/2,c_{0,1}=\alpha^{Chen}-1,c_{-1,1}=\left(1-\alpha^{Chen}\right)/2,$$

$$d_{0,0}=-\beta^{Chen},d_{1,0}=\beta^{Chen}-1,d_{1,1}=\left(1-\beta^{Chen}\right)/2,d_{0,1}=\beta^{Chen},d_{-1,1}=\left(1-\beta^{Chen}\right)/2,$$

$$b_{0,0}=c^{Chen}/2,b_{1,0}=d^{Chen},b_{1,1}=f^{Chen},b_{0,1}=d^{Chen},b_{-1,1}=f^{Chen},$$

where $\alpha^{Chen}$, $\beta^{Chen}$, $c^{Chen}$, $d^{Chen}$ and $f^{Chen}$ are the optimization coefficients in Chen (2014a), and Equation (4) becomes the ADM scheme in Chen (2014a). Therefore, the two previous L-F domain FD schemes can be derived from equation (4) as special cases.

## L-F domain optimal FD operator

Three types of L-F domain FD schemes (Figure 2), including the traditional standard 9-point scheme (Jo et al., 1996), 7-point scheme (Fan et al., 2018), and 9-point scheme (Fan et al., 2021), are considered. The latter two FD schemes are mainly used in discontinuous-grid FD modeling with a grid spacing ratio of N = 2 and N = 3 respectively. No matter in. Regardless of the frequency or L-F domain, the key issue of discontinuous-grid FD modeling is dealing with the wavefield in the transition region of the fine-to-coarse grid, where artificial reflections may be generated without proper FD schemes. Details can be found in Fan et al. (2018) and Fan et al. (2021).

According to the optimization method in the previous section, $a_{m,n}$ and $b_{m,n}$ are first determined by optimizing equation (9) and $c_{m,n}$ and $d_{m,n}$ are identified by optimizing equation (10). All the optimization coefficients are

calculated in this paper using the constrained nonlinear optimization function fmincon in MATLAB. For the traditional standard 9-point scheme, the range of propagation angle is [0, π/2] and that of and are both [0,0.15]. Given the different R = 1.0 and 2.0, 12 independent coefficients of the standard 9-point scheme are obtained, as shown in Table 1. The dispersion curves of R = 1.0 and 2.0 are shown in Figures 3 and 4, respectively. The left and right columns are normalized numerical phase velocity surfaces $v_r/v$ and $v_i/v$ normalized numerical attenuation propagation velocity surfaces , respectively. Each row from top to bottom represents different propagation angles.

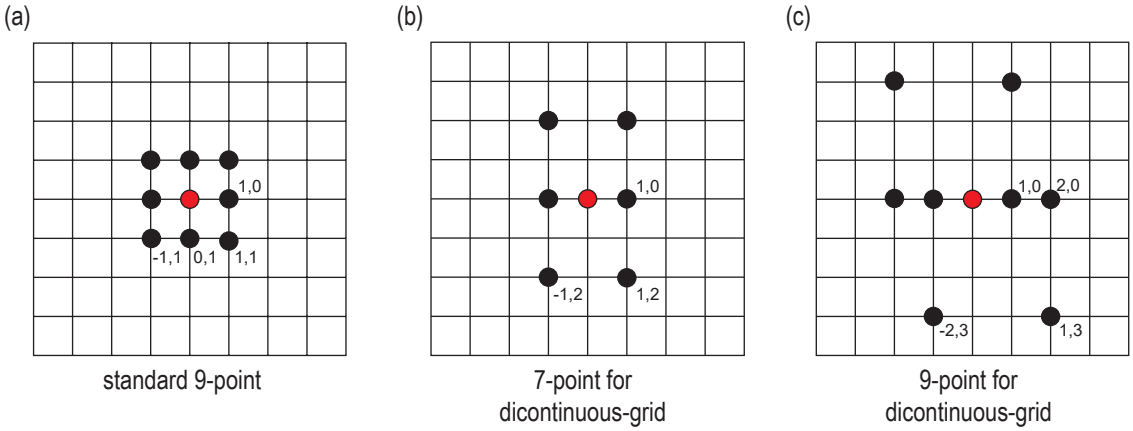


**Figure 2. Three types of L-F domain FD scheme: (a) standard 9-point scheme, (b) 7-point scheme used in discontinuous-grid modeling with N = 2, and (c) 9-point scheme used in discontinuous-grid modeling with N = 3**

Only the case of R = 1.0 is considered for 7- and 9-point schemes that are used in discontinuous-grid FD modeling. $\tilde{k}_r$ and $\tilde{k}_i$ are set within [0, 0.10] and [0, 0.08], respectively. The resulting optimization coefficients are shown in Tables 2 and 3, and the corresponding dispersion surfaces are presented in Figures 5 and 6. The 7-point scheme has high accuracy because the involved gridpoints in the 7-point scheme are evenly distributed and close to the central gridpoint. In addition, regardless of the 7- or 9-point scheme, the dispersion error along the x-axis (i.e., $\theta = 90^\circ$) is smaller than that along

**Table 1. Optimized coefficients for standard 9-point L-F FD operators with different R values.**

| ***R*** | 1.0 | 2.0 |
|---|---|---|
| $b_{1,0}$ | 8.08469167884408E-02 | 7.71428796302654E-02 |
| $b_{0,1}$ | 8.08469167976356E-02 | 7.93314493514118E-02 |
| $b_{1,1}$ | 1.41531741254217E-09 | 6.17863506001517E-09 |
| $b_{-1,1}$ | 3.11961627591611E-03 | 6.86999278161673E-03 |
| $c_{1,0}$ | 8.42727716796900E-01 | 8.79555711326816E-01 |
| $c_{0,1}$ | -1.54664414471238E-01 | -1.18767513169156E-01 |
| $c_{1,1}$ | 7.79803151005666E-02 | 6.00277549629858E-02 |
| $c_{-1,1}$ | 7.81498802136955E-02 | 5.74611945463850E-02 |
| $d_{1,0}$ | -1.54664251764376E-01 | -1.54628497601172E-01 |
| $d_{0,1}$ | 8.42727879499684E-01 | 8.44941639790144E-01 |
| $d_{1,1}$ | 7.79802222748798E-02 | 7.73591224866439E-02 |
| $d_{-1,1}$ | 7.81498476639072E-02 | 7.80782162165015E-02 |

**Table 2. Optimized coefficients for 7-point L-F FD operators with R=1.0 (Δ*x*=Δz).**

| ***R*** | 1.0 |
|---|---|
| $b_{1,0}$ | 8.94138245623699E-03 |
| $b_{1,2}$ | 4.26312120638903E-02 |
| $b_{-1,2}$ | 4.26312120638903E-02 |
| $c_{1,0}$ | 9.93952211862394E-01 |
| $c_{1,2}$ | 9.39952712675884E-04 |
| $c_{-1,2}$ | 9.39952712675884E-04 |
| $d_{1,0}$ | -2.43619026037833E-01 |
| $d_{1,2}$ | 1.24055968646330E-01 |
| $d_{-1,2}$ | 1.24055968646330E-01 |

**Table 3. Optimized coefficients for 9-point L-F FD operators with R=1.0 (Δx=Δz).**

| ***R*** | 1.0 |
|---|---|
| $b_{1,0}$ | 7.90153933735926E-01 |
| $b_{2,0}$ | 2.92253643104417E-02 |
| $b_{1,3}$ | 2.66922360527131E-02 |
| $b_{-2,3}$ | 6.19832512659083E-02 |
| $c_{1,0}$ | -3.18375148152123E+00 |
| $c_{2,0}$ | 1.04480922957390E+00 |
| $c_{1,3}$ | 4.86295404413319E-04 |
| $c_{-2,3}$ | 3.27969634340508E-04 |
| $d_{1,0}$ | -2.31732710677734E-01 |
| $d_{2,0}$ | 3.55951478988712E-03 |
| $d_{1,3}$ | 7.34796852868217E-02 |
| $d_{-2,3}$ | 3.69264435072868E-02 |

the z-direction due to the involvement of additional gridpoint nodes in the x-direction by the 7- and 9-point FD stencils in Figures 2b and 2c.

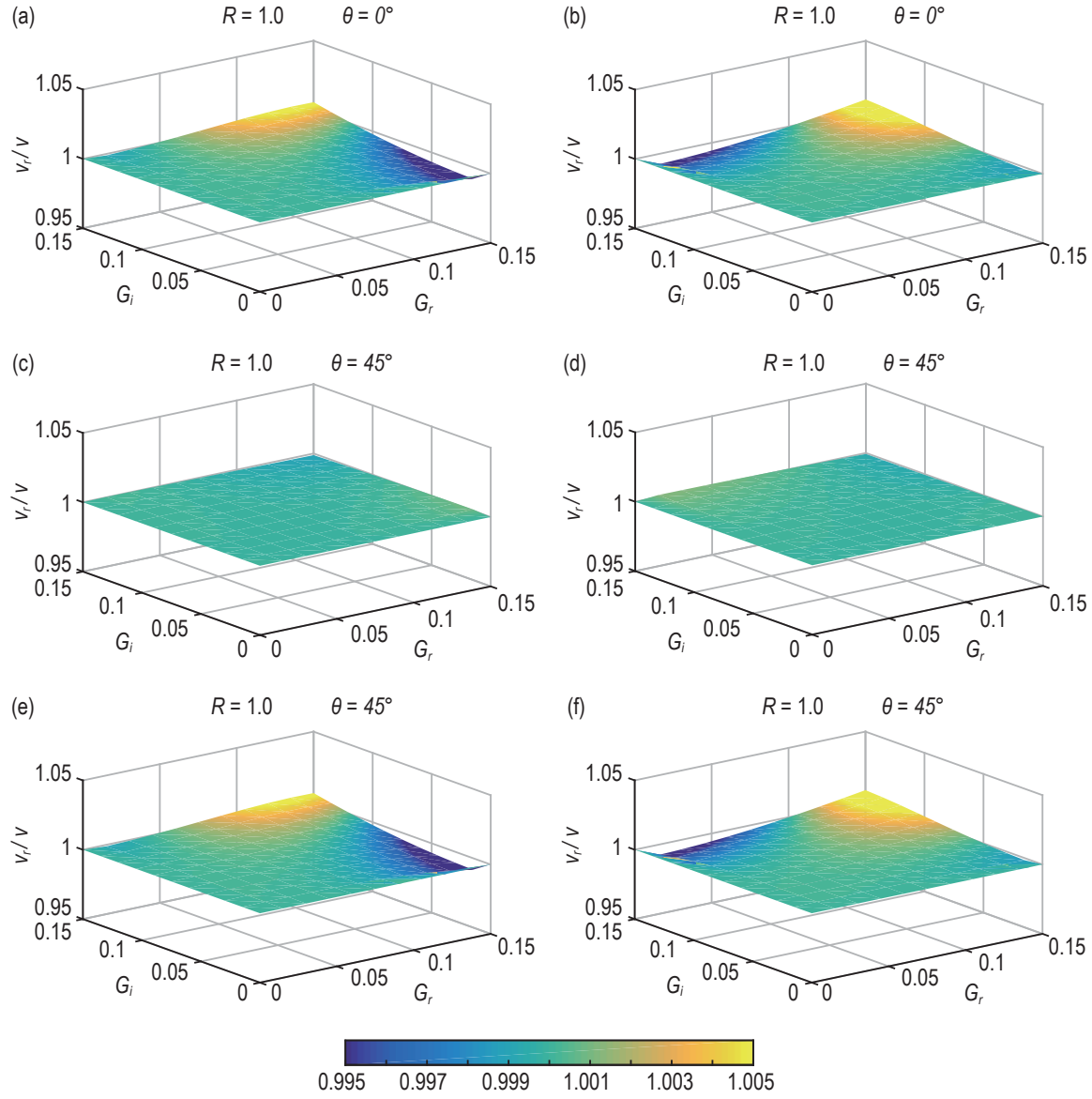


**Figure 3. Dispersion surfaces for the traditional standard 9-point scheme when R = 1.0. x- and y-axes denote the number of gridpoints per wavelength ($G_r$) and per pseudo-wavelength ($G_i$), respectively. (a), (c), and (e) are the normalized numerical phase velocity ($v_r/v$) surfaces and (b), (d), and (f) are normalized numerical attenuation propagation velocity ($v_i/v$) surfaces. Three rows from top to bottom denote propagation angles of $\theta = 0^\circ, 45^\circ, 90^\circ$.**

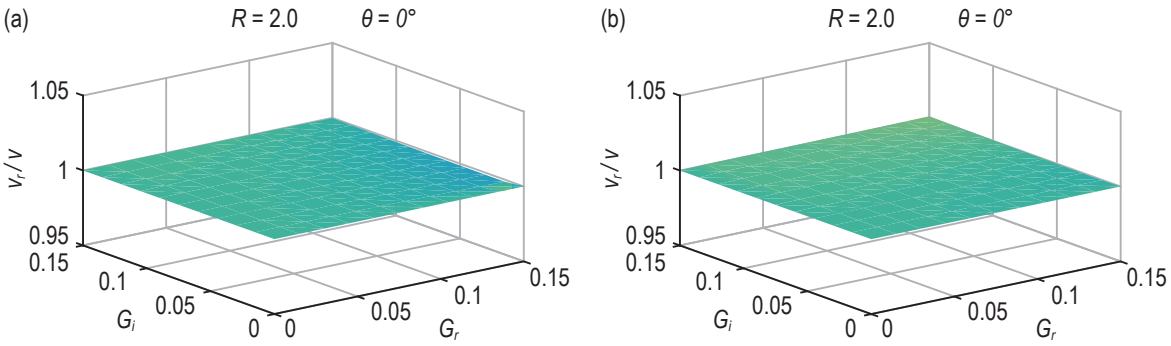

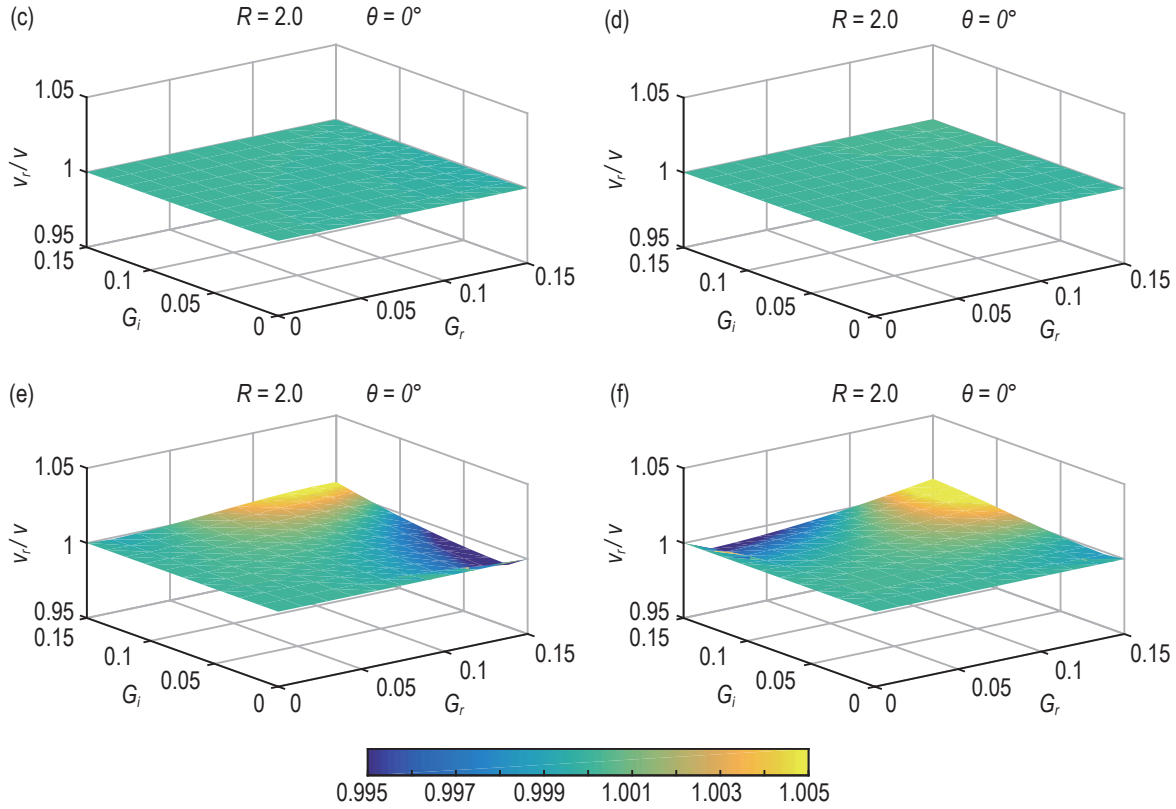


**Figure 4. Dispersion surfaces for the traditional standard 9-point scheme when R = 2.0. (a–f) are similar to Figures 3a–3f.**

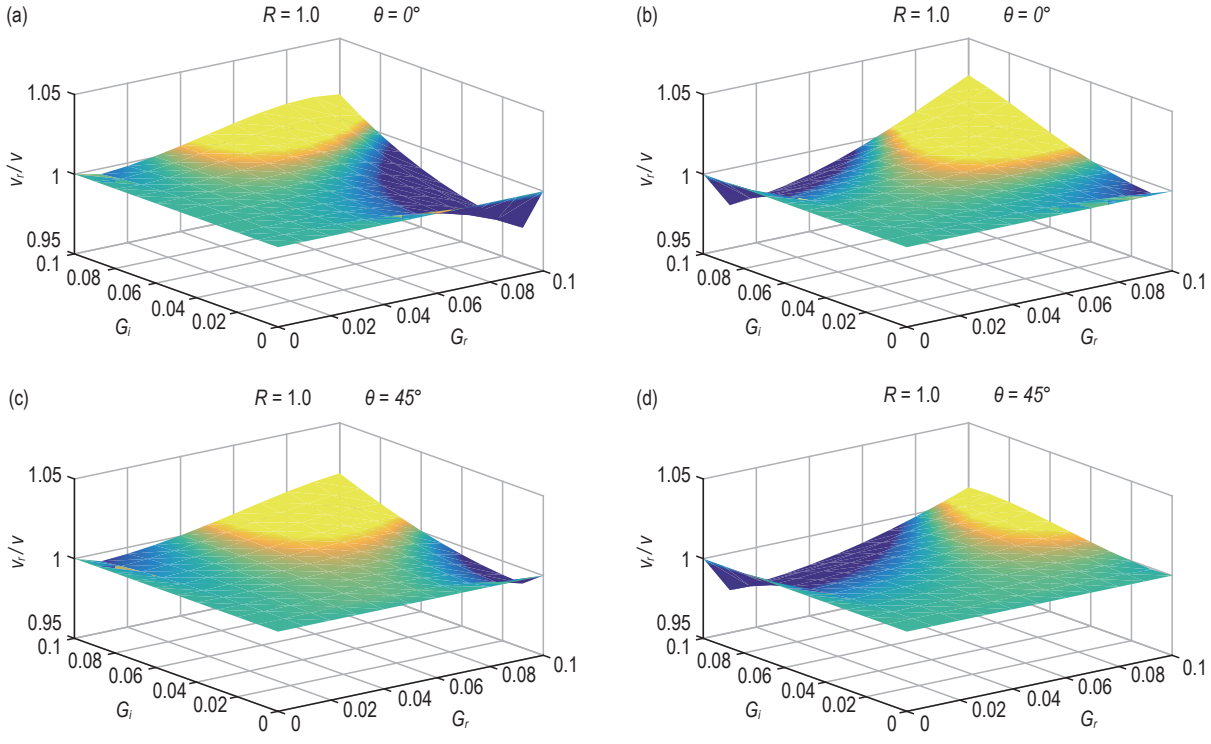

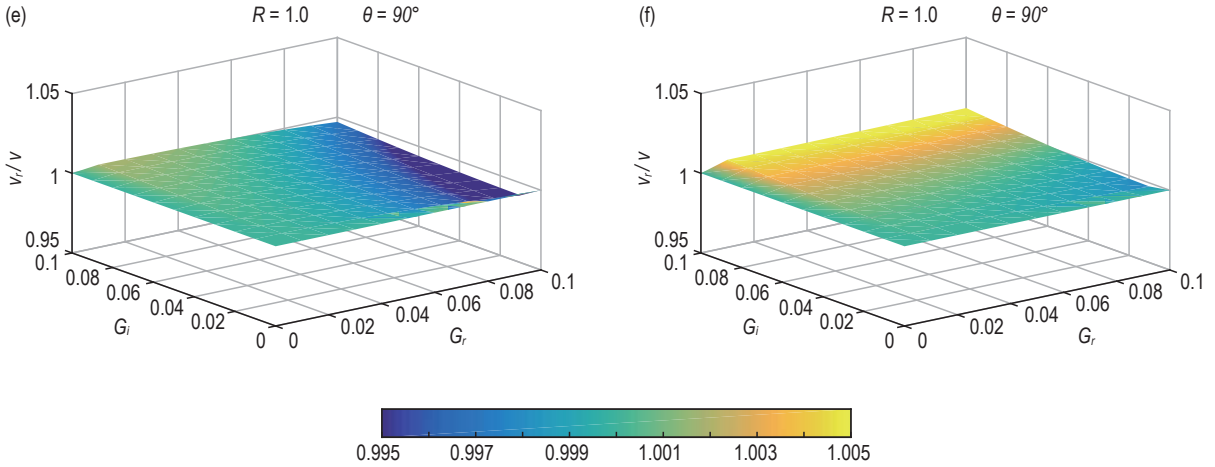


**Figure 5. Dispersion surfaces for the 7-point scheme when *R* = 1.0, which is usually used in discontinuous-grid modeling with N = 2. (a–f) are similar to Figures 3a–3f.**

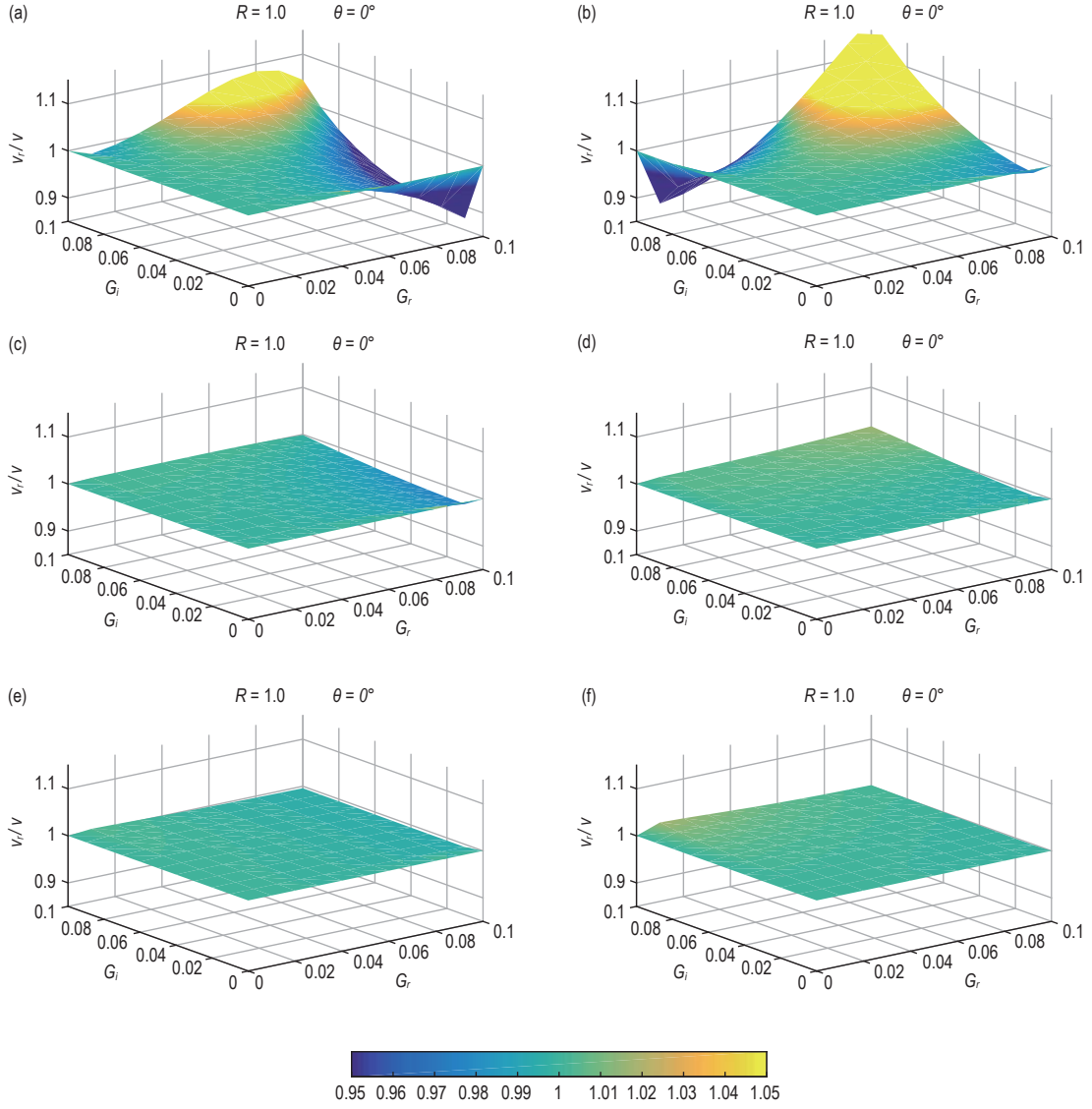


**Figure 6. Dispersion surfaces for the 9-point scheme when R = 1.0, which is usually used in discontinuous-grid modeling with N = 3. (a–f) are similar to Figures 3a–3f.**

# Numerical Experiments

Three numerical experiments are presented to validate the three aforementioned types of L-F domain FD schemes. The first is a homogenous model, which adopts the standard 9-point scheme. The second one is a layered model, in which the discontinuous-grid FD method is used with 7- and 9-point schemes in the transition region. The last one is a complex model, and the optimal method is compared with ADM (Chen, 2014a). All three numerical tests are implemented under a single complex frequency point, and the source is a 25 Hz Ricker wavelet. PML is used as the four absorption boundaries.

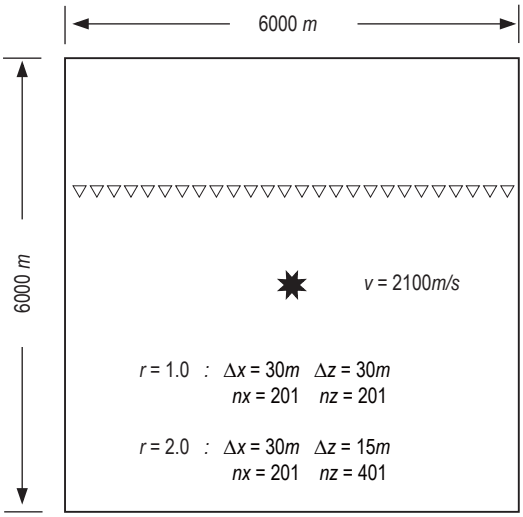


**Figure 7. Homogeneous model has a size of 6000 × 6000 m and an acoustic velocity of $v$ = 2100 m/s. The star denotes the source located at (3000, 3000) m, and the inverted triangle indicates a row of receivers at a depth of $z$ = 1800 m.**

1.0 and $R$ = 2.0, respectively, and the red curve is the analytical solution. The comparison results reveal that the three waveform results are highly consistent.

## Layered Model

The L-F domain discontinuous-grid FD modeling method is verified in a flat three-layer model in the second numerical experiment. The 7- and 9-point FD schemes with N = 2 and N = 3 are used in the fine-to-coarse grid transition regions, respectively. The model is shown in Figure 9 with a size of 3000 × 6300 m and acoustic velocities of 1000, 2000, and 6000 m/s in three different layers. Two velocity interfaces are located at depths of 1475 and 3250 m (dashed lines in Figure 9), and the source is located at (1500, 1000) m.

## Homogeneous Model

First, the L-F domain standard 9-point scheme is validated in a homogenous model. The model has a size of 6000 × 6000 $m$, a source at (3000, 3000) m, and a row of receivers at depth $z$ = 1800 m. The acoustic velocity is $v$ = 2100 m/s. The model is discretized by either a square or a rectangle grid. The former uses equal grid space with $\Delta x = \Delta z$ = 30 m (R = 1.0), and the resulting grid is 201 × 201. The second uses a rectangular grid with $\Delta x$ = 30 m, $\Delta z$ = 15 $m$ ($R$ = 2.0), and the resulting grid is 201 × 401. The L-F domain optimization coefficients listed in Table 1 are used, and the simulation is implemented under a single complex frequency of $\sigma = 10\pi$, $\omega = 5\pi$. Next, the waveforms recorded by a row of receivers are compared with that from the analytical solution (Chen, 2014a). The comparisons are shown in Figure 8, where the blue and green curves denote the results from $R$ =

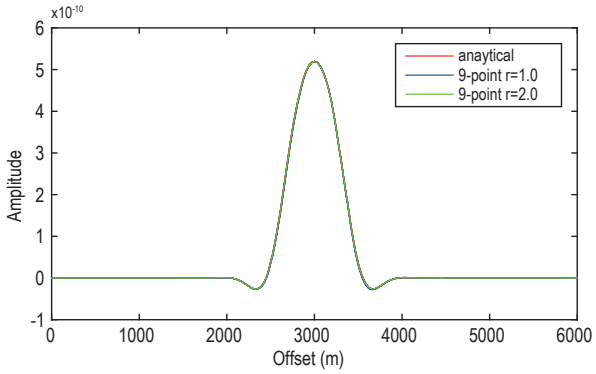


**Figure 8. Waveform comparison in the L-F domain in the homogeneous model. The blue and green curves indicate the simulated waveforms using the standard 9-point scheme with square and rectangle grids, respectively. The red curve indicates the analytical waveform.**

The model is discretized by uniform and discontinuous grids. The former uses a small grid spacing of $\Delta x = \Delta z$ = 5$m$ in the entire model, and its simulated waveforms are regarded as the benchmark to verify the results from discontinuous-grid modeling. The latter uses a small grid spacing of $\Delta x = \Delta z$ = 5$m$ m in the shallow part, a large grid spacing of $2\Delta x$ and $2\Delta z$ in the middle part, and the largest grid spacing of $6\Delta x$ and $6\Delta z$ in the deep part (i.e., discontinuous-grid spacing ratio N = 2 for the first interface and N = 3 for the second interface). The thickness of the three different grided regions are 1500, 1800, and 3000 m (denoted by the solid lines in Figure 9), and the resulting gridpoints of each region are 601 × 301, 301 × 180, and 101 × 100, respectively. Three rows of receivers are placed at a depth of $z$ = 400, 2500, and

5400 m in different layers. The L-F domain simulation is performed under the single complex frequency of σ = 10 π, ω = 5 π, and the resulting waveforms from uniform- and discontinuous-grid modeling are shown in Figure 10. The waveforms from the L-F domain uniform- and discontinuous-grid modeling have high consistency, but those recorded in shallow parts have high consistency.

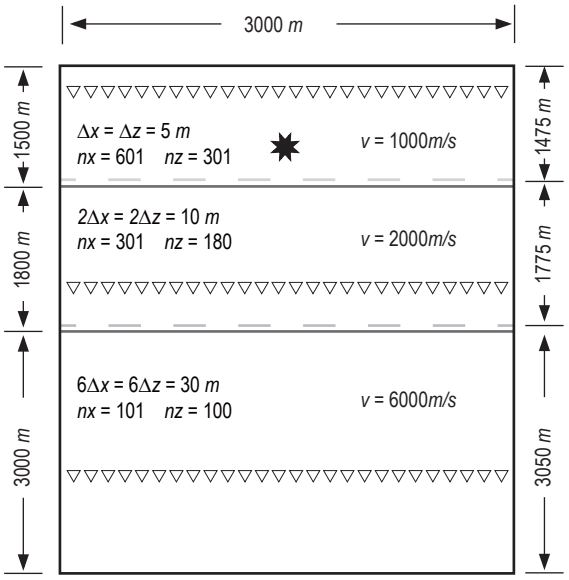


**Figure 9. Flat three-layer model has a size of 3000 × 6300 m and acoustic velocities of 1000, 2000, and 6000 m/s in each layer. Two dashed lines indicate velocity interfaces located at depths of 1475 and 3250 m. Two solid lines indicate discontinuous-grid interfaces located at depths of 1500 and 3300 m. The star denotes the source at (1500, 1000) m, and three rows of inverted triangles denote receivers at depths of 400, 2500, and 5400 m.**

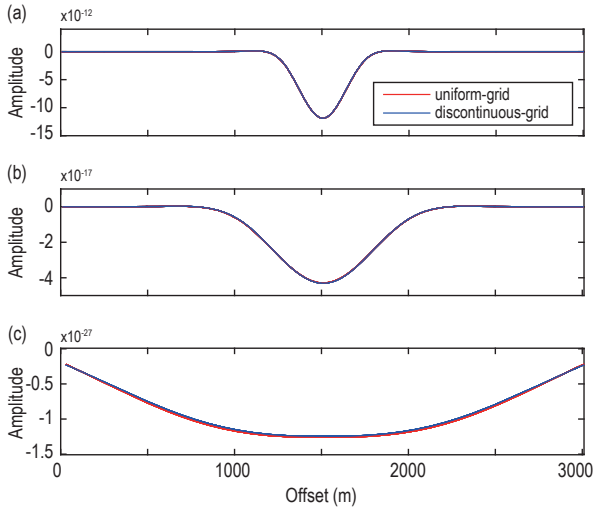


**Figure 10. Waveform comparisons between uniform- and discontinuous-grid modeling in the L-F domain in the three-layer model. (a), (b), and (c) are received waveforms by three rows of receivers in different layers in Figure 9. The red and blue curves result from the L-F domain uniform- and discontinuous-grid modeling, respectively.**

## Complex Model

The Marmousi model is chosen for the latest test to compare the optimal method with the ADM FD modeling of Chen (2014) in the L-F domain. The model is shown in Figure 11 with a size of 5000 × 2800 m, and the source is located at (2500, 50)m. The entire model uses a uniform grid with a spacing of $\Delta x = \Delta z = 5\ m$. A row of receivers is placed at a depth of $z = 50\ m$. The wavefield is computed at two complex frequency points of $s = \pi + 5\pi i$ and $s = \pi + 20\pi i$, where Figure 12 shows wavefield snapshots in the L-F domain.

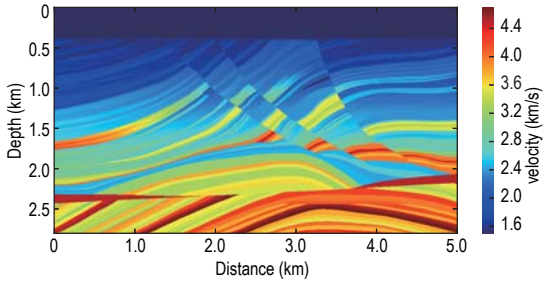


**Figure 11. Marmousi model**

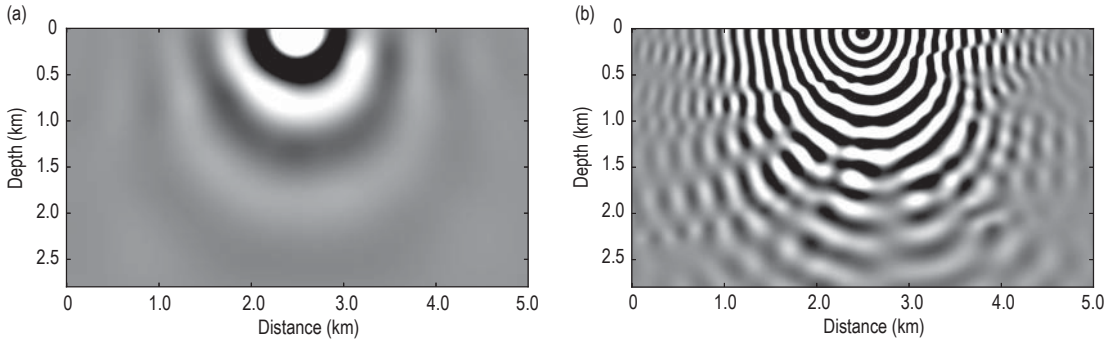


**Figure 12. L-F domain wavefield snapshots at single complex frequencies of (a) $s = \pi + 5\pi i$ and (b) $s = \pi + 20\pi i$.**

Figure 13 demonstrates the seismograms recorded by a row of receivers at the same depth as the source. The seismograms are compared with the results of the ADM 9-point scheme of Chen (2014a) to validate its accuracy. Figure 13 shows the red solid and blue dashed curves, which are the results from the ADM 9-point scheme and the proposed method, respectively. The two L-F domain seismograms are highly consistent, which proves that the optimal method has approximate accuracy with the ADM 9-point scheme. However, the L-F domain FD scheme has a flexibility stencil; therefore, it can be applied to discontinuous-grid modeling to reduce computation costs.

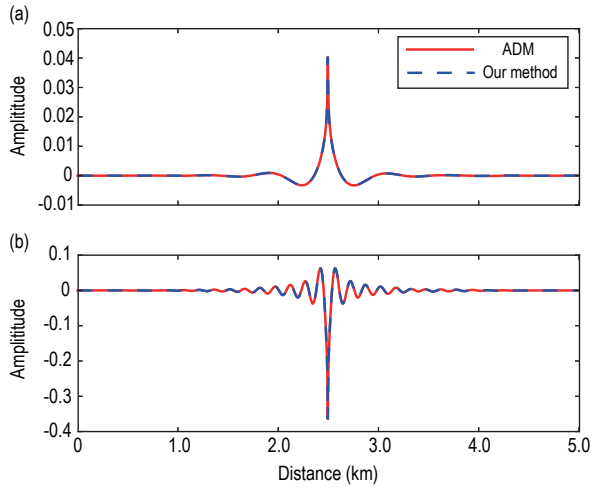


**Figure 13. L-F domain seismograms at a row of receivers, which is located at depth z = 50 m. The complex frequency of (a) is $s = \pi + 5\pi i$ and (b) is $s = \pi + 20\pi i$. The red solid lines are due to the ADM 9-point scheme, and the blue dashed lines are obtained from the proposed method in this paper.**

## Conclusion

An optimal FD scheme with a flexible and centrosymmetric-gridpoint stencil is developed on the basis of the 2D L-F domain acoustic wave equation. The optimization coefficients of the L-F domain FD operator can be determined using the L-F domain dispersion analysis method (i.e., minimizing the phase error of the normalized numerical phase and attenuation velocities). The optimal L-F domain FD method can work with traditional standard 9-point scheme and 7- and 9-point schemes, which are typically used in discontinuous-grid modeling. The optimization coefficients for these schemes are presented, and the accuracy is validated in three numerical experiments. These experiments demonstrate that the optimal L-F domain FD method not only has high accuracy but can also adapt to square, rectangle, and discontinuous grid to reduce the computation cost.

## Acknowledgment

This work was supported by the National Natural Science Foundation of China (no. 41604037), Natural Science Foundation of Hubei Province (no. 2022CFB125), the Open Fund of Key Laboratory of Exploration Technologies for Oil and Gas Resources (Yangtze University), Ministry of Education (no. K2021-09) and College Students' Innovation and Entrepreneurship Training Program (no. 2019053).

## References

Bae, H. S., Shin, C., Cha, Y. H., Choi, Y., and Min, D. J., 2010 . 2D acoustic-elastic coupled waveform inversion in the Laplace domain: Geophysical Prospecting, **58**(6), 997–1010.

Bleistein, N., Cohen, J. K., and Hagin, F. G., 1987, Two and one-half dimensional Born inversion with an arbitrary reference: Geophysics, **52**(1), 26–36.

Cao, S.-H., and Chen, J.-B., 2012, A 17-point scheme and its numerical implementation for high-accuracy modeling of frequency-domain acoustic equation: Chinese Journal of Geophysics, **55**(10), 3440–3449.

Cao, S.-H., and Chen, J.-B., 2014, Studies on complex frequencies in frequency domain full waveform inversion (in Chinese): Chinese Journal of Geophysics, **57**(7), 2302–2313.

Chen, J.-B, 2012, An average-derivative optimal scheme for frequency-domain scalar wave equation. Geophysics, **77**(6), T201–T210.

Chen, J.-B., 2014a, Dispersion analysis of an average-derivative optimal scheme for Laplace-domain scalar wave equation: Geophysics, **79**(2), T37–T42.

Chen, J.-B, 2014b, Laplace-Fourier-domain dispersion analysis of an average derivative optimal scheme for scalar-wave equation: Geophysical Journal International, **197**(3), 1681–1692.

Chen, J.-B, 2016, Numerical dispersion analysis for three-dimensional Laplace-Fourier-domain scalar wave equation: Exploration Geophysics, **47**(2), 158–167.

Chen, J.-B., and Cao, J., 2016, Modeling of frequency-domain elastic-wave equation with an average-derivative optimal method: Geophysics, **81**(6), T339-T356.

Chen, J.-B., and Cao, J., 2018, An average-derivative optimal scheme for modeling of the frequency-domain 3D elastic wave equationAn optimal scheme for elastic equation: Geophysics, **83**(4), T209–T234.

Choi, Y., and Alkhalifah, T., 2011, Source-independent time-domain waveform inversion using convolved wavefields: Application to the encoded multisource waveform inversion: Geophysics, **76**(5), R125–R134.

Fan, N., Xie, X.-B., Zhao, L.-F., Tang, X.-G., and Yao, Z.-X., 2021, An optimal frequency-domain finite-difference operator with a flexible stencil and its application in discontinuous-grid modeling: Geophysics, **86**(3), T143–T154.

Fan, N., Zhao, L.-F., Xie, X.-B., Tang, X.-G., and Yao, Z.-X., 2017, A general optimal method for 2D frequency-domain finite-difference solution of scalar wave equation: Geophysics, **82**(3), T121–T132.

Fan, N., Cheng, J.-W., Qin, L., Zhao, L.-F., Xie, X.-B., and Yao, Z.-X., 2018a, An optimal method for frequency-domain finite-difference solution of 3D scalar wave equation (in Chinese): Chinese Journal of Geophysics, **61**(3), 1095–1108.

Fan, N., Zhao, L.-F., Xie, X.-B., and Yao, Z.-X., 2018b, A discontinuous-grid finite-difference scheme for frequency-domain 2D scalar wave modeling: Geophysics, **83**(4), T235–T244.

Gu, B., Liang, G., and Li, Z., 2013, A 21-point finite difference scheme for 2D frequency-domain elastic wave modeling: Exploration Geophysics, **44**(3), 156–166.

Ha, W., Chung, W., Park, E., and Shin, C., 2012, 2-D acoustic Laplace-domain waveform inversion of marine field data: Geophysical Journal International, **190**(1), 421–428.

Hustedt, B., Operto, S., and Virieux, J., 2004, Mixed-grid and staggered-grid finite-difference methods for frequency-domain acoustic wave modeling: Geophysical Journal International, **157**(3), 1269–1296.

Jo, C.-H., Shin, C., and Suh, J. H., 1996, An optimal 9-point, finite-difference, frequency-space, 2-D scalar wave extrapolator: Geophysics, **61**(2), 529–537.

Min, D.-J., Shin, C., Kwon, B.-D., and Chung, S., 2000, Improved frequency-domain elastic wave modeling using weighted-averaging difference operators: Geophysics, **65**(3), 884–895.

Operto, S., Brossier, R., Combe, L., Métivier, L., Ribodetti, A., and Virieux, J., 2014, Computationally efficient three-dimensional acoustic finite-difference frequency-domain seismic modeling in vertical transversely isotropic media with sparse direct solver: Geophysics, **79**(5), T257–T275.

Operto, S., Virieux, J., Amestoy, P., L'Excellent, J.-Y., Giraud, L., and Ali, H. B. H., 2007, 3D finite-difference frequency-domain modeling of visco-acoustic wave propagation using a massively parallel direct solver: A feasibility study: Geophysics, **72**(5), SM195–SM211.

Operto, S., Virieux, J., Ribodetti, A., and Anderson, J. E., 2009, Finite-difference frequency-domain modeling of viscoacoustic wave propagation in 2D tilted transversely isotropic (TTI) media: Geophysics, **74**(5), T75–T95.

Pratt, R. G., 1999, Seismic waveform inversion in the frequency domain, Part 1: Theory and verification in a physical scale model: Geophysics, **64**(3), 888–901.

Pratt, R. G., Shin, C., and Hick, G., 1998, Gauss–Newton and full Newton methods in frequency–space seismic waveform inversion: Geophysical Journal International, **133**(2), 341–362.

Pratt, R. G., and Worthington, M., 1988, The application of diffraction tomography to cross-hole seismic data: Geophysics, **53**(10), 1284–1294.

Shin, C., and Cha, Y. H., 2008, Waveform inversion in the Laplace domain: Geophysical Journal International, **173**(3), 922–931.

Shin, C., and Cha, Y. H., 2009, Waveform inversion in the Laplace-Fourier domain: Geophysical Journal International, **177**(3), 1067–1079.

Shin, C., Koo, N.-H., Cha, Y. H., and Park, K.-P., 2010, Sequentially ordered single-frequency 2-D acoustic waveform inversion in the Laplace–Fourier domain: Geophysical Journal International, **181**(2), 935–950.

Shin, C., Min, D.-J., Marfurt, K. J., Lim, H. Y., Yang, D., Cha, Y., et al., 2002, Traveltime and amplitude calculations using the damped wave solution: Geophysics, **67**(5), 1637–1647.

Sirgue, L., and Pratt, R. G., 2004, Efficient waveform inversion and imaging: A strategy for selecting temporal frequencies: Geophysics, **69**(1), 231–248.

Song, Z.-M., Williamson, P. R., and Pratt, R. G., 1995, Frequency-domain acoustic-wave modeling and inversion of crosshole data: Part II—Inversion method, synthetic experiments and real-data results: Geophysics, 60(3), 796-809.

Tang, X., Liu, H., Zhang, H., Liu, L., and Wang, Z., 2015, An adaptable 17-point scheme for high-accuracy frequency-domain acoustic wave modeling in 2D constant density media: Geophysics, **80**(6), T211–

T221.
Tarantola, A., 1984, Inversion of seismic reflection data in the acoustic approximation: Geophysics, **49**(8), 1259–1266.
Um, E. S., Commer, M., and Newman, G. A., 2012, Iterative finite-difference solution analysis of acoustic wave equation in the Laplace-Fourier domain: Geophysics, **77**(2), T29–T36.
Vigh, D., and Starr, E. W., 2008, Comparisons for waveform inversion, time domain or frequency domain : 78th Annual International Meeting, SEG, Expanded Abstracts, 1890–1894.
Virieux, J., and Operto, S., 2009, An overview of full-waveform inversion in exploration geophysics: Geophysics, **74**(6), WCC1–WCC26.
Yang, P., Gao, J., and Wang, B., 2015, A graphics processing unit implementation of time-domain full-waveform inversion: Geophysics, **80**(3), F31–F39.
Yang, Q., and Mao, W., 2016, Simulation of seismic wave propagation in 2-D poroelastic media using weighted-averaging finite difference stencils in the frequency–space domain: Geophysical Journal International, **208**(1), 148–161.
Zhang, H., Liu, H., Liu, L., Jin, W., and Shi, X., 2014, Frequency domain acoustic equation high-order modeling based on an average-derivative method (in Chinese): Chinese Journal of Geophysics, **57**(5), 1599–1611.

**Jing-Yu Wang** received her Bachelor's degree in Geophysics from Yangtze University in 2022. Currently she is pursuing a Master's degree at Chiba University. She focuses on the study of seismicity.
Email: jingyu2000816@outlook.com

**Na Fan** received the B.S. degree in geophysics from Wuhan University, Wuhan, China, in 2010, and the Ph.D. degree from the Institute of Geology and Geophysics, Chinese Academy of Science, Beijing, China, in 2015. She is currently an Associate Professor at the Yangtze University, Wuhan. Her research interests include seismic data processing, forward modeling, inversion, and imaging.
Email: fanna@yangtzeu.edu.cn

**Xue-Fei Chen** received her Ph.D. degree from Chengdu University of Technology. She is currently a Lecturer at the Yangtze University. Her major is exploration and information technology, and her main research interests are reservoir prediction and geological interpretation.
Email: chenxf@yangtzeu.edu.cn

**Shou-Rui Zhong** obtained a Bachelor's degree in Geophysics from Yangtze University in 2021 and is currently pursuing a Master's degree in Solid Earth Geophysics at China University of Geosciences (Wuhan) with a research focus on ambient noise seismology.
Email: zsr@cug.edu.cn.'

**Bo-Yu Li** obtained his Bachelor's degree in Geophysics from Yangtze University in 2021. His major is geophysics, and his main research interests are rock physics and seismic exploration.
Email: lby092014@163.com

**Dan Li** obtained her Bachelor's degree in Geophysics from Yangtze University in 2022. Currently she is pursuing a Master's degree at China University of Geosciences (Beijing). Her major is earth exploration and information technology, and main research interest is seismic data processing.
Email: ld187270360@163.com.

**Gang Zhao** received his Bachelor's degree in Geophysics from Yangtze University in 2022. He currently works for Henan Oilfield Branch of China Petroleum and Chemical Corporation.
Email: zg20201109@163.com